REPORT DOCUMENTATION PAGE

Form Approved
OMB No. 0704-0188

The public reporting burden for this collection of information is estimated to average 1 hour per response, including the time for reviewing instructions, searching existing data sources, gathering and maintaining the data needed, and completing and reviewing the collection of information. Send comments regarding this burden estimate or any other aspect of this collection of information, including suggestions for reducing the burden, to the Department of Defense, Executive Service Directorate (0704-0188). Respondents should be aware that notwithstanding any other provision of law, no person shall be subject to any penalty for failing to comply with a collection of information if it does not display a currently valid OMB control number.

PLEASE DO NOT RETURN YOUR FORM TO THE ABOVE ORGANIZATION.

1. REPORT DATE *(DD-MM-YYYY)*
09-27-2011

2. REPORT TYPE
Final Report

3. DATES COVERED *(From - To)*
04/01/2008 - 07/31/2011

4. TITLE AND SUBTITLE
Combining Imaging and Non-Imaging Observations for Improved Space-Object Identification

5a. CONTRACT NUMBER

5b. GRANT NUMBER
FA9550-08-1-0151

5c. PROGRAM ELEMENT NUMBER

6. AUTHOR(S)
Prasad, Sudhakar, Brady, David, and Plemmons, Robert

5d. PROJECT NUMBER

5e. TASK NUMBER

5f. WORK UNIT NUMBER

7. PERFORMING ORGANIZATION NAME(S) AND ADDRESS(ES)
University of New Mexico
MSC05 3480, Scholes Hall, Room 327
1 University of New Mexico
Albuquerque, NM 87131

8. PERFORMING ORGANIZATION REPORT NUMBER

9. SPONSORING/MONITORING AGENCY NAME(S) AND ADDRESS(ES)
Air Force Office of Scientific Research
875 North Randolph Street
Suite 325, Rm 3112
Arlington, VA 22203

10. SPONSOR/MONITOR'S ACRONYM(S)
AFOSR/RSE

11. SPONSOR/MONITOR'S REPORT NUMBER(S)
AFRL-OSR-VA-TR-2012-0241

12. DISTRIBUTION/AVAILABILITY STATEMENT
Approved for Public Release

13. SUPPLEMENTARY NOTES

14. ABSTRACT

During the theoretical effort, we proposed and tested (i) a new sparsity model for man-made space objects and its use, via a new spectral-correlation approach, to segment their material components, (ii) the use of 2D segment-boundary data for multiple poses of a man-made space object to recover its 3D shape, (iii) derived new fundamental results involving statistical information and Bayesian error bounds for characterizing the performance of reconstruction algorithms; and (iv) computed Fisher information to quantify the value of object support for spatial-bandwidth extension beyond diffraction-limited observations. The experimental/instrumentation-related accomplishments include (i) new CASSI instrumentation for supplying multiple frames of high-resolution, broad-band hyperspectral image (HSI) data in compressive form, (ii) supplying CS data from CASSI to the WFU-based researchers to test their algorithms for HSI reconstructions, and (iii) developing a push-broom variant of CASSI. The computational accomplishments include (i) developing and testing new joint segmentation and spectral recovery algorithms, (ii) developing an alternating LS algorithm for segmenting and reconstructing the full HSI datacube, and (iii) a sparse nonnegative matrix under-approximation approach.

15. SUBJECT TERMS
Compressive spectral imaging, hyperspectral datacube reconstruction, information theory, Bayesian estimation and detection, space-object identification, segmentation and material identification

16. SECURITY CLASSIFICATION OF:			17. LIMITATION OF ABSTRACT	18. NUMBER OF PAGES	19a. NAME OF RESPONSIBLE PERSON
a. REPORT	b. ABSTRACT	c. THIS PAGE			Sudhakar Prasad
U	U	U	SAR	26	19b. TELEPHONE NUMBER *(Include area code)* 505-277-5876

Reset

Final Report

Combining Imaging and Non-imaging Observations for Improved Space-Object Identification

April 1, 2008 - July 31, 2011

Prof. S. Prasad, PI
(with contributions from the Co-PI's,
Prof. R. Plemmons, Wake Forest U. and Prof. D. Brady, Duke U.)

September 27, 2011

Grant No. FA9550-08-1-0151

Abstract

This document represents the final report on the various scientific activities and accomplishments relating to Grant No. FA9550-08-1-0151 over its period of performance, April 1, 2008 - July 31, 2011.

The accomplishments may be subdivided according to the project's theoretical, experimental, and post-processing/computational objectives. Among the theoretical accomplishments, we list

- a new model for a sparse representation of man-made space objects and its use, via a new spectral-correlation approach, to segment their material components;
- the use of 2D segment-boundary data for multiple poses of a man-made space object to recover its 3D shape;
- new fundamental results involving statistical information and Bayesian error bounds for characterizing the performance of reconstruction algorithms, and feature-extraction and estimation fidelity; and
- the use of Fisher information and the associated Cramer-Rao lower bound on estimator variance to characterize the value of a prior knowledge of object support for spatial-bandwidth extension beyond diffraction-limited observations.

The experimental/instrumentation-related accomplishments include

- new CASSI instrumentation for supplying multiple frames of high-resolution, broad-band hyperspectral image (HSI) data in compressive form;
- supplying CS data from CASSI to the WFU-based researchers to test their algorithms for efficiency, accuracy, and robustness of HSI reconstructions from single-frame and multi-frame data; and
- developing a push-broom variant of CASSI for comparing ground truth HSI data with reconstructions from compressively sensed (CS) CASSI data.

Finally, the computational/mathematical accomplishments include

- developing and testing a number of new joint segmentation and spectral recovery algorithms for uncompressed HSI data;
- developing an alternating LS algorithm for segmenting and reconstructing the full HSI datacube from compressed CASSI data and testing it on both simulated and real experimental data; and
- a sparse nonnegative matrix under-approximation approach that uses a sparsity constraint to process HSI data.

1 Overall Project Objectives

To place the project accomplishments in proper perspective, we first present its originally proposed objectives. Specifically, we aimed

1. to develop fundamental mathematical models and system design methodologies supporting the identification of space objects from multi-modal data;

2. to simulate and design laboratory experiments to demonstrate novel compressive spectral coherence imaging approaches for SOI;

3. to develop an information-theoretic toolbox of concepts and metrics to analyze system performance; and

4. to offer numerical approaches that yield the most computationally efficient algorithms for post-processing the data generated by those methods.

The project was subdivided according to its theoretical, experimental, and mathematical/computational thrusts, with the three collaborating institutions, UNM, Duke, and WFU, being the respective leaders of these three thrusts. We begin with a summary of UNM's work in meeting the theoretical objectives of this effort, followed by Duke U.'s work leading to an experimental realization of compressive spectral sensing in the presence of atmospheric turbulence, and end with WFU's contributions to algorithm development for various compressive sensing reconstruction strategies. The work in these three research thrust areas has resulted in a series of important publications and invited/contributed presentations at professional meetings in computational imaging and data analysis. These are listed in Sections 3-5 of this report.

2 Summary of Overall Project Accomplishments

The four originally proposed objectives of the effort were largely achieved over the project duration. In this report we provide only a summary description of the project accomplishments, leaving the many technical details of a fuller description to the project-supported publications that are cited at appropriate places below and are publicly accessible. Our technical accomplishments may be summarized as follows:

2.1 Sparse Hyperspectral Object Model

We proposed and exploited a unique model of sparsity of satellite objects. Such objects may be regarded quite accurately as being composed of homogeneous material segments with uniform spectral and brightness characteristics except possibly near the segment boundaries. This implies a relatively small number of characteristic parameters when compared with the vast number of spectral-spatial voxels in the hyperspectral datacubes of such objects. This observation was exploited to recover the values of these parameters and thus reconstruct the whole hyperspectral datacube from both compressive and non-compressive noisy spectral data. A number of papers published by the project team chronicle this development over the project duration.

2.2 A Spectral Correlation Approach for Segmentation and Spectral Recovery

Hyperspectral datasets typically contain far more information than needed for a typical remote sensing task of material identification, segmentation, and composition. A typical solar-illuminated man-made satellite consists of a relatively small number of geometrical primitives and materials with unique spectral reflectance signatures. This implies a highly correlated hyperspectral data cube, which may be idealized as a low-rank sum of terms, each expressible in a spatial-spectral factorized form. The high degree of spectral correlation within each spatial segment of the object admits a simple moving-averages (MA) approach for identifying the material components and their spatial boundaries, as we have recently demonstrated (Li, Ng, Plemmons, Prasad and Zhang, 2010). This approach works equally well with a less idealized form of the data cube that allows for arbitrary, non-uniform values within the support of each material component.

In the MA approach, we cross-correlate the spectral traces at different spatial pixels in the dataset with the spectral traces of different materials, either picked from a sufficiently exhaustive database of spectra or extracted from the HSI dataset itself. To improve the SNR of the normalized cross-correlation, we average it over a small cell, say 2x2 or 4x4 square pixels in size, that we move over the full spatial-pixel array in the HSI dataset. As the averaging cell moves, the normalized correlation varies between 0 and 1. The value 1 signals a perfect match between the test trace and the spectral trace of pixels inside the moving cell, while a much smaller value indicates poorly matched or mismatched spectra. By repeating this calculation with different test traces, we can then segment the various components and also identify their spectra.

To demonstrate this approach, we used the hyperspectral image (HSI) data cube of the Hubble space telescope (HST) that was simulated in Zhang, Wang, Plemmons, and Pauca (2010) for demonstrating low-rank tensor methods on HSI data. Figure 1 shows a noisy HST spatial brightness distribution (PSNR=20) in the mid-spectral band. The effectiveness of the moving-averages approach in segmenting the eight different material components of the HST from its HSI data cube is easily seen in the eight panels of Fig. 2.

2.3 Surface Shape Recovery and Pose Estimation

The unique relationship among the two-dimensional (2D) projections of a curve fixed on a rigidly rotating three-dimensional (3D) object, with one projection per pose, implies that those projections contain precise information about the object shape and size parameters as well as the Euler angles describing the poses assumed by the object as it rotates. We can exploit this observation for a rotating 3D space object by following the kinematical evolution of its segment boundaries whose 2D image-plane projections can be determined, e.g., by the moving-averages approach. If each material component of the object has a specific but simple geometry, we can idealize the components in terms of simple geometrical primitive shapes, such as spheres, ellipsoids, cylinders, cones, parallelepiped, triangles, tetrahedra, etc, drawn from a database of shapes. Given the 2D image-plane projections of a curve and a certain primitive shape, we construct a fit-to-data L2 functional to optimize for the shape parameters, Euler angles for each pose, the 3D body coordinates of points on the

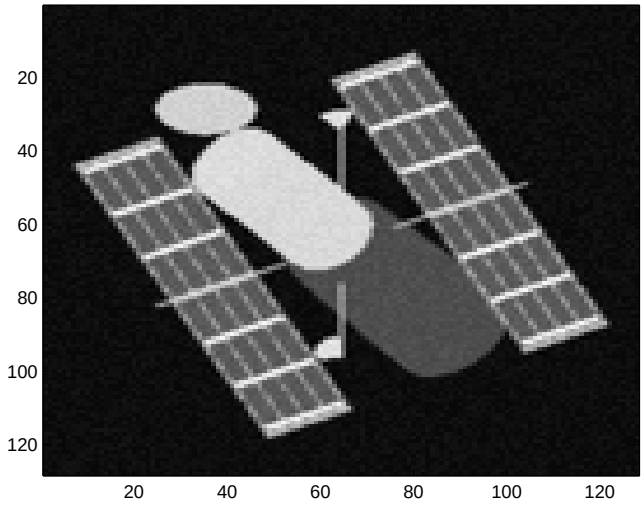

Figure 1: The spatial brightness distribution of the simulated HST in the middle spectral channel

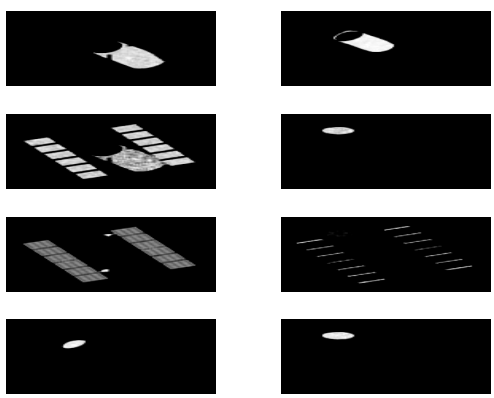

Figure 2: Map of the spectral cross-correlation function for the eight different material traces used in the construction of the HST datacube.

curve, and the rotation matrix for each pose. For this highly nonlinear problem, we use a block coordinate descent algorithm to alternately optimize for each set of parameters in an iterative way. And by searching exhaustively through a database of primitives, we can infer the specific primitive shape and its size parameters that correspond most closely to the time series of observed 2D projections of a specific boundary.

In our initial studies (Prasad and Zhang, 2010), through forward models we simulated the 2D projections of curves on an ellipsoid and a cylinder at two different poses, from which we sought to recover the original parameters and body coordinates used in the simulation. The

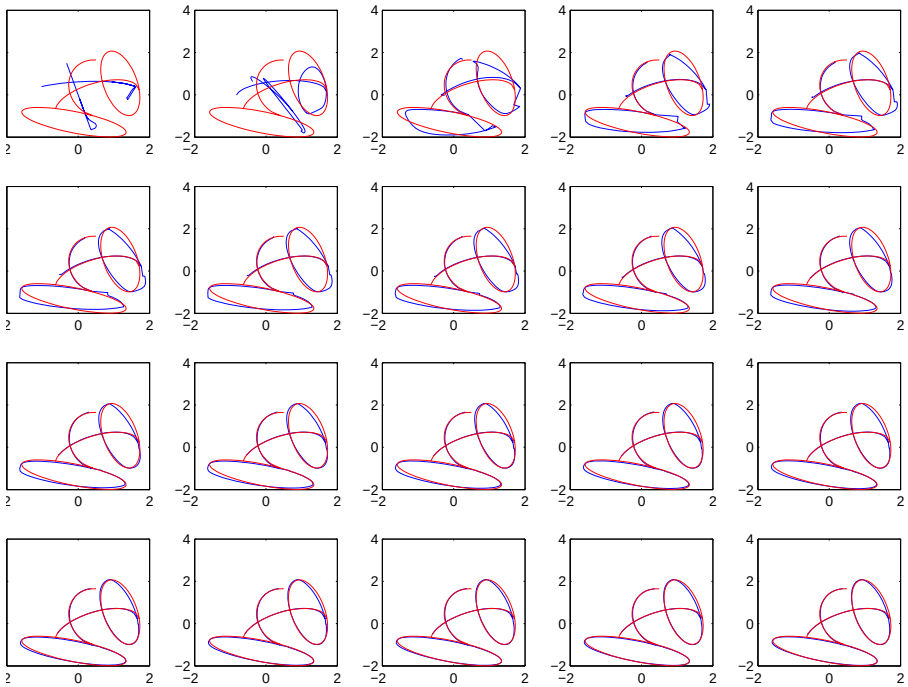

Figure 3: Two curves on an ellipsoid of certain orientation, shown in red, fitted to an ellipsoid via an iterative fitting algorithm

results have been very promising. We have shown, in particular, that with just a few poses of the rotating surface and its segment boundaries, the fit to wrong shapes across segment boundaries can be heavily discriminated against. Even with just two poses, we could infer the correct shape from similar looking projections while discriminating against other shapes, as we see in Figs. 3 and 4. Here the two poses of a curve on an ellipsoid are shown in red. In Fig. 3 we fitted the two poses to a correct ellipsoidal surface shape, and determined the parameters of the ellipsoid iteratively. One can see that after about 10 iterations of the fitting alorithm, the fit, shown by blue curves, is quite good. By contrast, when the curves are fitted to a cylinder, which is a wrong shape, the fit does not improve at all over the first 20 iterations and beyond, as shown in Fig. 4. Estimated shape parameters and Euler angles, not given here, are also quite close to the original when the correct shape was tried.

This approach can be exploited to devise a recursive algorithm for determining the surface geometry of the entire object as it rotates to reveal its complete surface over a certain observation period.

Surface shapes can be further constrained by well resolved polarimetric observations of the reflected sunlight. Under recently obligated AFOSR funding, we are now developing, testing, and extending our technique further to include spectro-polarimetric image data in order to achieve a more comprehensive characterization of the surface properties via purely optical observations. We are also exploring the use of superquadric parametric surfaces to

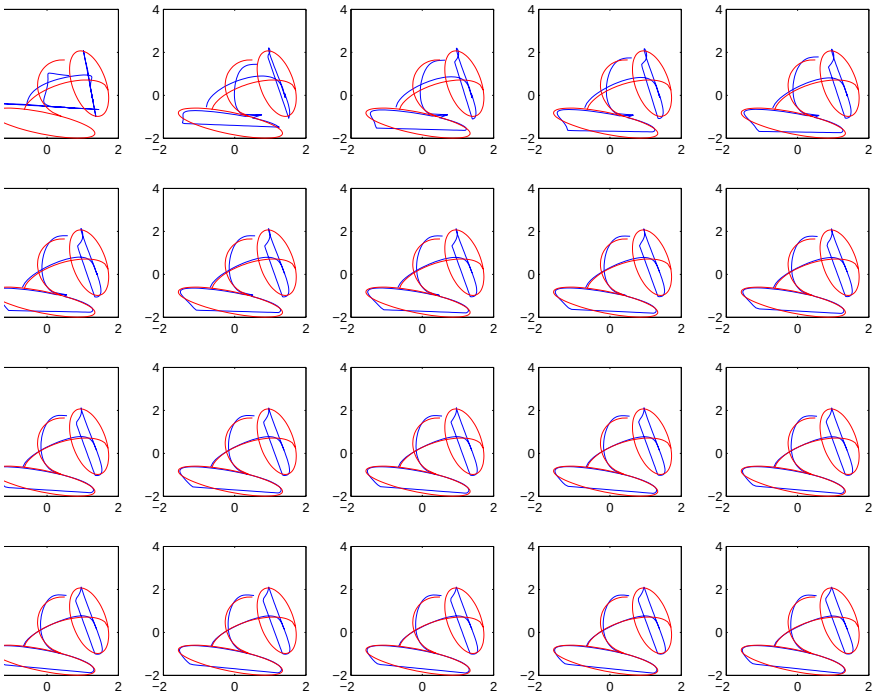

Figure 4: Two curves on an ellipsoid of certain orientation, shown in red, fitted to an ellipsoid via an iterative fitting algorithm

simulate more general surfaces than our simple primitive shapes have to offer.

2.4 Fundamental Relations between Statistical Information and Bayesian Error Bounds

A number of mathematical relations connecting statistical information (SI) with Bayesian error analysis were developed and analyzed under the grant effort. In particular, we have studied just how the minimum mean-squared error (MMSE) of Bayesian estimation and minimum probability of error (MPE) in Bayesian M-ary hypothesis testing bound the equivocation entropy, which represents the loss of information in a communication channel such as an imaging system. These quantities were calculated for the problem of localizing an unresolved source with sub-diffractive error in the presence of image blur and detection noise. This calculation is evidently quite relevant for locating faint space objects, such as space debris and small GEO satellites that are unresolved in the space imaging setting. The details of this work may be found in Prasad (2011) (submitted to JOSA A), Prasad and Narravula, 2011, and some unpublished work (Narravula and Prasad); here we present only important results.

Relations Involving MPE, Statistical Equivocation, and Mutual Information An important result in this context is the following that relates the MPE for M-ary detection to a generalized version of the equivocation entropy (GEE) of statistical information theory:

$$P_e^{(min)} = 1 - \mathbb{E}_x \left\{ \exp\left[-\int_1^\infty \frac{dn}{n^2} H_n(\mathcal{H}|X=x) \right] \right\}, \tag{1}$$

where the GEE of nth order, $H_n(\mathcal{H}|X=x)$, is defined as

$$H_n(\mathcal{H}|X=x) = -\sum_{m=1}^{M} P_n(m|x)\, \ln P_n(m|x), \tag{2}$$

in terms of the following n-indexed PDF for a specified data value x:

$$P_n(m|x) = \frac{P^n(m|x)}{\sum_m P^n(m|x)}, \quad m = 1, \ldots, M. \tag{3}$$

From this exact result, there follow a number of well known bounds on the MPE, namely the Santhi-Vardy and the Renyi bounds involving the ordinary equivocation entropy related more directly to the MI.

The MI can be shown to be bounded below by a logarithmic function of MMSE, as shown by Seidler nearly forty years ago. However, there is also an upper bound related to the MPE, given data X, that we have derived recently, namely

$$I(\Theta; X) \leq H(\Theta) + \mathbb{E}_X \left[\max_m \{p(\theta_m|X)\} \, \log \max_m \{p(\theta_m|X)\} \right], \tag{4}$$

where $H(\Theta)$ is the signal entropy. The tightness of the upper bound (4) is directly determined by the smallness of the average amount of spill-over of any posterior probability mass function

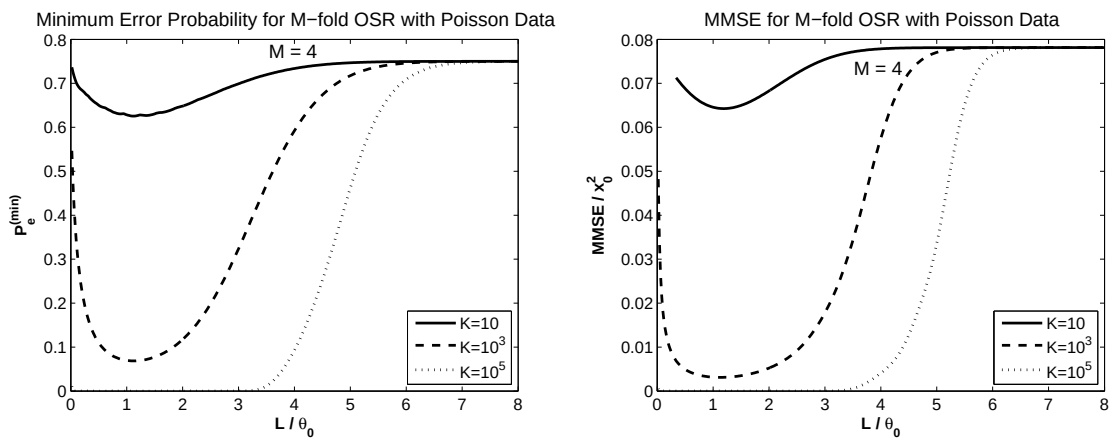

(a) (b)

Figure 5: (a) Minimum MPE and (b) MMSE for resolving the source position vs. image pixel width (in units of diffraction-limited pixel width) for $M = 4$ for three different source strengths, $K = 10$, 10^3, and 10^5, in the Poisson shot-noise model.

(PMF), $p(\theta_m|X)$, into neighboring decision regions, namely $I_{mm'}$, $m' \neq m$, that we can also use to relate the MPE to MMSE (see next paragraph). For this reason, this bound is expected to be quite tight for highly sensitive Bayesian detectors, A number of other new bounds on the MI in terms of the MPE have also been obtained, but because of space considerations we are not presenting them here.

Relation between MPE and MMSE and Application to Source Location For a highly sensitive detector, *i.e.,* when the SNR is high, the MMSE and MPE are both related directly to the probability for incorrect inference, namely that one of the incorrect $M-1$ parameter values gave rise to the data. If $I_{mm'}$ denotes the probability of inferring the parameter value $\theta_{m'}$, given the parameter value θ_m, $m \neq m'$, then the MMSE and MPE are both related to this quantity as

$$\begin{aligned} \text{MMSE} =& \frac{1}{2}\sum_m \sum_{m'} (\theta_m - \theta_{m'})^2 \left(I_{mm'} + I_{m'm}\right) + O(\epsilon^2) \\ P_e^{(min)} =& \frac{1}{2}\sum_m \sum_{m' \neq m} \left(I_{mm'} + I_{m'm}\right), \end{aligned} \tag{5}$$

where terms of smaller order can be neglected in the first expression in the limit of large SNR. This close connection between the MPE and MMSE is seen in Fig. 5 for a single-pixel point-source localizer for photon-limited imaging.

We have derived a tight upper bound on the MMSE (Narravula and Prasad, unpublished), which makes it possible to calculate the MMSE approximately in the most general situation thus rendering it numerically highly amenable. This bound,

$$\text{MMSE} \leq \mathbb{E}[\delta\hat{\theta}(k) - \delta\theta]^2, \tag{6}$$

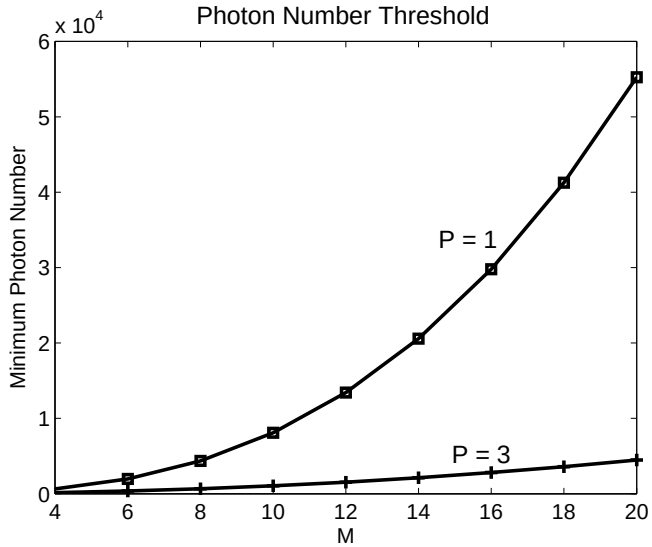

Figure 6: Plot of the source-strength threshold, K_{min}, vs. the degree of localization, M, for the one-pixel imager (square symbols) and the three-pixel imager (+ symbols).

where the prefix δ denotes linear deviations, $\delta A = A - \mathbb{E}(A)$, and $\hat{\theta}$ is *any* estimator of θ, can be made tight by a variational approach in which one minimizes the RHS of this inequality over a parametric family of test estimators. Use of this bound enables us to derive the photon-number thresholds needed to achieve point-source localization with sub-diffractive error, a type of optical super-resolution. The minimum photon number needed for M-fold reduction in localization error relative to diffractive localization has an expected M^2 form when several pixels worth of image data are exploited for this purpose, but a single pixel image requires a far steeper photon threshold of form $M^{2.77}$, as displayed in Fig. 6 below.

2.5 Statistical Information in Reconstruction Algorithms

Another application of our SI based performance metrics has involved the study of information recovered by an algorithm that exploits image data with or without any post-processing constraints such as the knowledge of object support. We have generated plots of mutual information (MI), namely the information in the ensemble of object scenes that is successfully transmitted by an imaging system to its reconstruction algorithm, with respect to varying amounts of detection noise and object support sizes to quantify information theoretic performance upper bounds. The imaging system of interest here has been one based on compressed sensing (CS) that performs projective measurements of masked image scenes involving two or more homogeneous surface components with different brightness values and then uses an algorithm to extract the position, size, and material signature (via pixel brightness differences between neighbors) of the components. We have showed that the MI obtained at the post-processing (algorithm) stage is lower than at the data stage, since any practical algorithmic reconstruction has finite errors of its own. However, the use of *a priori* knowledge, such as constraining the recovery of the center position of a component to a pre-specified

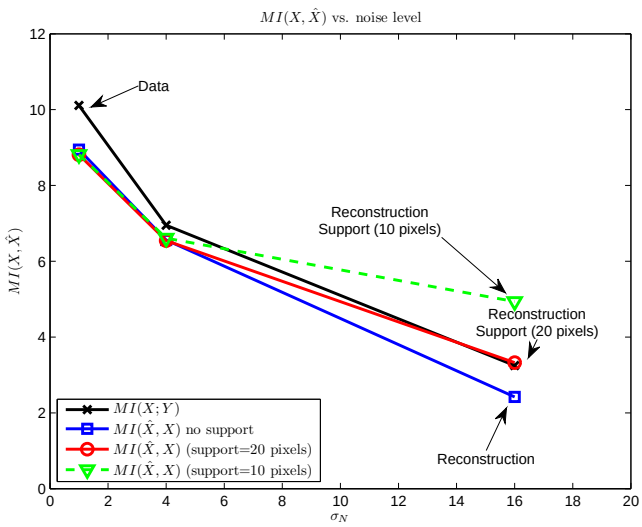

Figure 7: Plot of the mutual information (MI) vs. detection noise for the estimator algorithm, as compared to the MI in the CS data themselves.

rectangular support region about the true center, can be shown to improve the MI beyond that contained in the data alone if the support dimensions are chosen to be sufficiently small.

The following lower bound on the MI codifies this relationship between the MI, $I(X;\hat{X})$, and the variance of any estimator $\hat{X}$:

$$I(X;\hat{X}) \geq h(X) - h(X|\hat{X}) \leq \frac{1}{2}\mathbb{E}_{\hat{x}} \ln\left[2\pi e \mathbb{E}_{X|\hat{x}}(\hat{x}-X)^2\right], \tag{7}$$

where $h(X)$ is the differential entropy of the object, which is the maximum information that a perfect noiseless measurement can achieve. The fact that the estimator-recovered MI is smaller, in general, than the data-contained MI, $I(X;Y)$, is borne out in Fig. 7, where we plot the MI vs. detection noise for a readout-noise dominated compressive sensing system that extracts the center position of a square of given size inside another, larger square background. Note that by sharpening the prior constraint, in this case the support of the region of uncertainty of the center position of the inner square, we can more than overcome the loss of information caused by the detection noise when that is large.

2.6 Fisher-Information Analysis of Support-Assisted Optical and Digital Superresolution

Early in the project, we expolited Fisher information (FI) to characterize the extent of spatial-frequency extrapolation beyond the diffraction-limited optical bandwidth when the support of the object is known *a priori*. This support-assisted optical superresolution (OSR) phenomenon was analyzed for both 1D and 2D images by means of a Shannon-Nyquist type of sampling expansion in the spatial-frequency domain for a spatially limited object.

A 1D object $f(x)$ supported fully on the interval $[-L, L]$ has a Fourier-series expansion,

$$f(x) = \frac{1}{2L} \sum_{\ell=-\infty}^{\infty} F_\ell \exp(i\pi\ell x/L), \quad \text{with } F_\ell = \int_{-L}^{L} f(x) \ \exp\{-i2\pi[\ell/(2L)]x\} \ dx. \tag{8}$$

The Fourier transform (FT) of this expansion yields the full object spectrum, $F(u)$, in terms of its spatial-frequency samples, $F_\ell = F(u = \ell/2L)$, as

$$F(u) = \sum_{\ell=-\infty}^{\infty} F_\ell \ \mathrm{sinc}(2uL - \ell), \tag{9}$$

much like the usual Shannon-Nyquist expansion for a band-limited function in terms of its critical spatial samples. A similar but more involved expansion for 2D supported object brightness distribution may also be given at least for the case of rectangular and circular supports, the latter involving the Fourier-Bessel functions in place of the Fourier exponentials of Eq. (8).

For a one-dimensional (1D) imager with an idealized sensor array with no dead space between successive pixels and unit quantum efficiency, the pixel transfer function (PTF), $P(u)$, has the form, $P(u) = \delta w \ \mathrm{sinc}(u\delta w)$, where the sinc function is defined as $\mathrm{sinc}(x) \equiv \sin \pi x/(\pi x)$. For a clear aperture, the incoherent OTF is $(1 - |u|/B_0)$, B_0 being the optical bandwidth, the blurred image data at the kth pixel may be cast as an integral over the normalized frequency, $\bar{u} = u/B_0$, with all spatial variables scaled by the critical sampling interval, $1/(2B_0)$,

$$g_k = \frac{\chi}{2} \int_{-1}^{1} d\bar{u} \ \exp[i\pi\bar{u}(\bar{w}_k - \bar{t})] \ \mathrm{sinc}(\bar{u}\chi/2) \ (1 - |\bar{u}|) \ F(B_0\bar{u}) \ + \ n_k, \tag{10}$$

where $\chi = 2B_0\delta w$ is the ratio of detector-sampling and critical optical-sampling intervals, n_k is any additive sensor noise at the kth pixel, and $\bar{t}$ is any sub-pixel shift for an image. For $\chi < 1$, the detector oversamples the image while for $\chi > 1$ it undersamples the image.

When expansion (9) is substituted into Eq. (10), one sees that the image data are sensitive to object Fourier amplitudes F_ℓ that lie outside the optical bandwidth. This is a result of support-induced correlation of spatial frequencies inside to those outside the optical bandwidth of the imager. The Hermitian FI matrix for the sensitivity of the image data to the spectral amplitudes can be computed via a quasi-Gaussian approximation for the interesting case of Poisson image data in the presence of Gaussian additive sensor noise. The diagonal elements of the inverse of the FI matrix represent the minimum variance, also known as the Cramer-Rao lower bound (CRB), with which the real and imaginary parts of the corresponding spectral amplitude of the object may be estimated.

Figures 8 display the results of the CRB calculation for a 1D Gaussian-shaped object distribution for different data SNR values and for the space-bandwidth product (SBP) $Q \equiv 2B_0L = 20$. Note the sharp rise of the minimum variance of estimation when spectral samples increasingly beyond the band edge are considered. Indeed, the maximum extension of the SBP that can be achieved by means of support knowledge alone is of order 1, and depends logarithmically on the SNR.

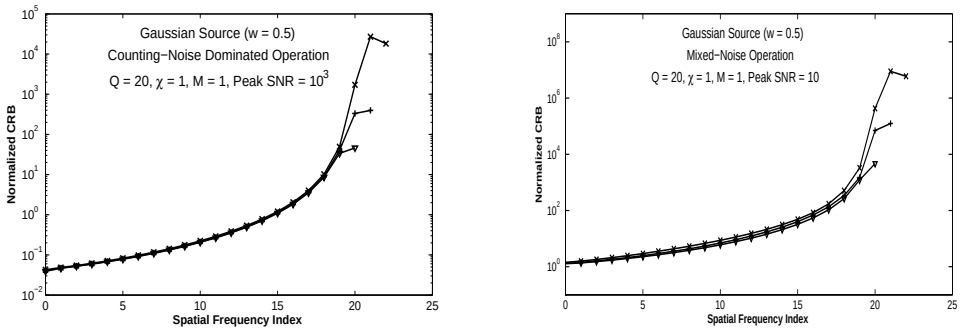

(a) $w = 0.5$, Peak SNR $= 10^3$ (b) $w = 0.5$, Peak SNR $= 10$

Figure 8: Normalized CRB for a Fourier sample plotted vs the index of the sample for $Q = 20$ and for two peak SNR values, 10^3 and 10.

The analysis based on the sampling expansions of the type (9) provides a unified treatment of both digital (DSR) and optical superresolution (OSR). Indeed, by analyzing a sequence of sub-pixel-shifted undersampled images one can show the minimum variance needed both to extract the critically sampled object brightness distribution and to even achieve optical-bandwidth extension to recover super-critically sampled, or superresolved, image data. These and 2D image DSR and OSR considerations were presented in great detail in three papers (Prasad and Luo, 2009 - all 3 papers listed in Sec. 3).

2.7 CASSI Instrumentation

We developed hardware to supply high resolution, broad bandwidth HSI data. This included a new instrument that is capable of acquiring multiple frames of uniquely coded data over 320nm-700nm. In addition, two detectors are available for data acquisition, one for UV-visible and another for higher frame-rate visible data. Lastly, a pushbroom variant of the CASSI system was developed for ground-truth data comparison with the compressively sensed CASSI data reconstructions.

The new CASSI instrument is shown in figure 9(a). The UV-visible detector shown can be swapped for a visible detector in a matter of minutes depending on the data acquisition needs. The UV detector has a quantum efficiency (QE) of 10% or less, while the visible detector has a QE of 55%, decreasing integration time by 5.5 times. This is particularly useful for dynamic scenes to decrease blur and increase frame rates for video applications. snapshots can be grouped for much higher resolution reconstructions. The relay lens was designed by Duke and custom built by Shanghai Optics.

The spectral range of the new instrument is 320-700nm divided over nearly 100 channels. The optics have also been completely custom designed for this specific application, greatly enhancing the performance of the instrument compared to the previous generation system. The camera is an Imperx Lynx IPX-4M15 UV-enhanced 2048x2048 monochrome detector (Visible: Allied Vision Technologies, Pike, 2048x2048). The aperture code is a random pattern lithographically etched on a chrome substrate by Photo Sciences with minimum

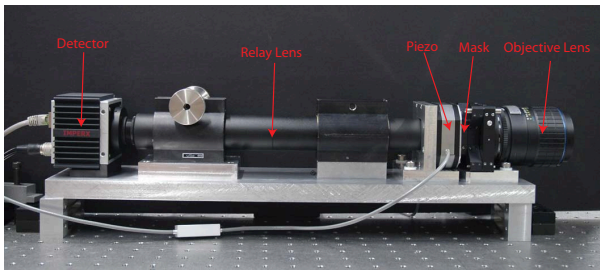

(a)

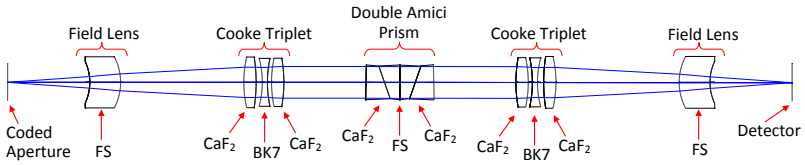

(b)

Figure 9: (a) Coded aperture spectral imager; (b) custom relay lens design.

features corresponding to two pixels or $14.8\mu m$. The aperture code is imaged onto the detector by the relay lens (custom fabrication by Shanghai Optics) and dispersed by a double amici prism. The aperture code is modulated by a piezo system (Newport Corporation) by up to 21 pixels on the detector. The objective lens was provided by Coastal Optics and is a true apochromat across the entire spectral range of the instrument.

At the heart of the system is a newly designed relay lens in figure 9(b) consisting of a modified Cooke triplet with field lenses. The system is symmetric around the prism, which is in the collimated space of the Cooke triplet. The $7.4\mu m$ pixels of the detector require an MTF of at least $67.6\ell p/mm$, while the aperture code size specifies the FOV. The entire spectral range of $300 - 700nm$ must be focused at all wavelengths, ideally being apochromatic. The difficulty with this wavelength range is that most glass types do not transmit below $350nm$. Fused silica (FS), calcium fluoride (CaF_2), and magnesium fluoride (MgF_2) transmit well below $300nm$, but because of MgF_2 being birefringent, it is not preferred by Shanghai Optics. With only two glass types, color correction is nearly impossible, so BK7 was considered, which for $5mm$ thickness transmits close to 90% above $320nm$. Compromising slightly at the lower UV significantly improved the MTF, with a minimum of $40 - 80\ell p/mm$ and most areas and wavelengths above $90\ell p/mm$.

Actual MTF measurements of the lens were done using an USAF resolution target, illuminated by 630nm (10nm bandpass) light. An Aptina MT9F002 monochrome 14 megapixel detector with $1.4\mu m$ pixels was used. The Air Force target measures the contrast transfer function (CTF), which can be converted to MTF approximately by multiplying the CTF by 0.785. This is only valid for higher frequencies, shown in figure 10(b), where frequencies below $60\ell p/mm$ are estimated and shown as the dashed line. This plot is only for the center of the lens. The 10nm bandpass region disperses about $6.6\mu m$, or 4.7 pixels on the Aptina detector in the horizontal direction, therefore, only MTF measurements were made for the horizontal bars. 20% contrast is observed at $144\ell p/mm$ and $67.6\ell p/mm$ is above 50%. This is in good agreement with the MTF shown from Zemax. Note in Zemax that the center

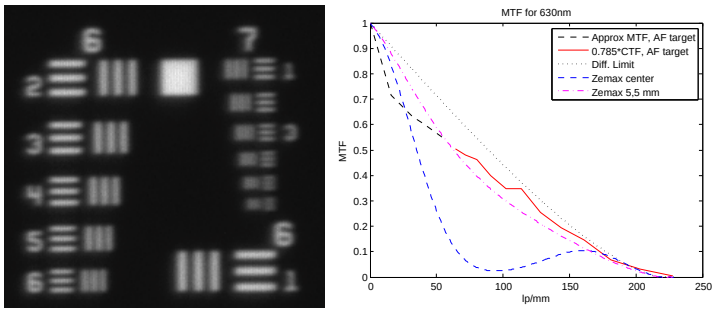

(a) (b)

Figure 10: 100% zoomed, cropped image of 1951 USAF target illuminated with 630nm light (10nm bandpass) imaged on an Aptina MT9F002 monochrome 14MP detector with 1.4μm pixels near the center of the field. There is approximately 5 pixels of dispersion in the horizontal direction; hence the vertical bars are more blurred.

MTF curve is worse than the five and seven millimeter curves since it was corrected over the entire field.

2.8 Experimental Results

Segmentation in collaboration with WFU researchers CASSI images of a color chart illuminated using Solux daylight 4700K lamps, shown in figure 11(a) are used for reconstructing both the color segments and their spectra. Since the spectral signatures within each segment are fairly uniform, the scene serves as a good candidate for testing the algorithm. For brevity, we only show the reconstructed colors in the second row as indicated by the red box in figure 11(b). The spectra of five colors excluding the purple are measured by an Ocean Optics (Dunedin, Florida) spectrometer. A total of 12 frames of SD-CASSI images are used for reconstructing a hyperspectral cube in 44 wavelength channels. Figure 11(c) shows the identified six segments. Clearly we are able to identify the sharp boundaries of the segments. For the accuracy of reconstructed spectra, we compared them with both references by the spectrometer in figure 12(a) and the reconstruction by TwIST in figure 12(b). Our results match almost identically with those by TwIST and show good agreement with the spectrometer references. Note that there has not been any calibration to accommodate for quantum efficiency, wavelength offset, and channel non-linearity. This accounts for the discrepancies shown in figure 12(b).

TwIST Reconstructions by the Duke group The UV-CASI system was then taken outside during an early summer afternoon when the UV-index was fairly high. Many flowers have ultraviolet and visible features, making an interesting target for spectral imaging. An RGB image of an Ox-Eye daisy (Heliopsis scabra) is shown below in figure 13(a), with a composite CASI image shown to the right. The visible RGB image shows no variation of the petals, but solid yellow color throughout. The CASI image in figure 13(b) shows that in the UV bands, a dark region surrounds the central part of the flower. Selected spectral channels are shown in figure 14 from 360nm to 702nm.

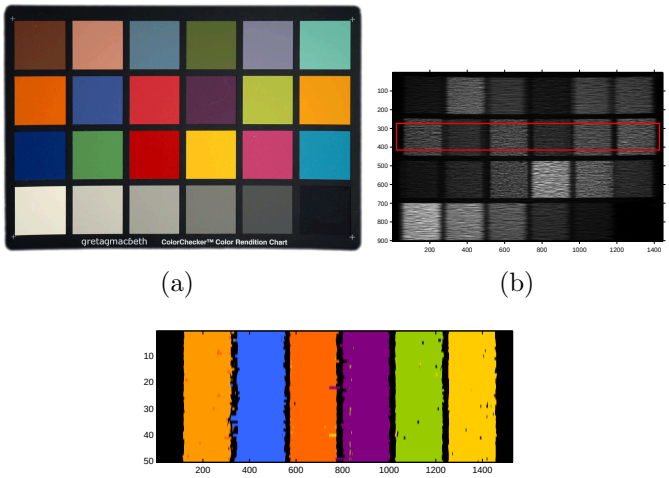

Figure 11: (a) RGB image of the Gretagmacbeth ColorChecker. (b) The original SD-CASSI image with the reconstructed area in the red rectangular box. (c) The reconstructed segments.

Two separate images were acquired with the CASI system since there are no bandpass filters available in the range of 320-700nm that strongly filter the IR bands. The visible band was imaged using a Baader UV/IR-cut filter, blocking below 400nm and above 680nm. The UV bands were imaged using a Badder U-filter Venus, blocking both the visible and IR. The Imperx camera is sensitive between 200nm and 1000nm, so blocking the 700-1000nm region is necessary. The reconstructions shown in figure 14 were done using TwIST and 20 uniquely coded frames for UV, and 24 frames for the visible.

Spectral accuracy Spectral features for a non-spatially varying scene are shown in figure 15. An Ocean Optics USB2000 spectrometer is compared to the CASSI system with a 1-pixel, slit and a random mask with 2-pixel features. The slit and random mask have similar spectra, with slight offsets from the ocean optics. The shown spectra are uncalibrated for the non-uniform quantum efficiency of the detector and optical transmission. The slit spectra for CASSI is directly read from the detector cross-section, while the random code data was reconstructed using TwIST as in figure 13(b). The random code has slightly better resolution than the slit, even though the slit is narrower than the minimum feature of the random code.

Pushbroom versus CASSI The coded aperture system can be compared to a reference data cube by swapping the coded aperture with a vertical slit and pushbrooming across the detector. The results for this experiment are shown in figure 16.

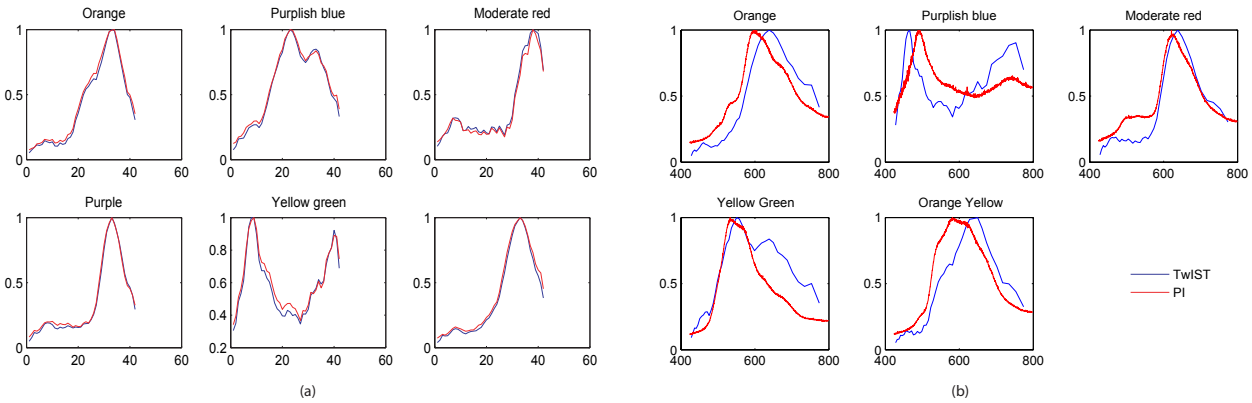

Figure 12: (a) The reconstructed spectra compared with reference by an Ocean Optics spectrometer. (b) The reconstructed spectra compared with reconstruction using TwIST.

(a) (b)

Figure 13: (a) Visible image taken with standard RGB camera. (b) CASSI image with UV channels on the left and visible on the right.

2.9 Joint segmentation and reconstruction methods

We developed numerical methods for the joint reconstruction and segmentation of spectral images taken by compressive sensing coded aperture snapshot spectral imagers (CASSI) (Zhang, Plemmons, Kittle, Brady and Prasad, 2011). In a snapshot, a CASSI captures a two-dimensional (2D) array of measurements that is an encoded representation of both spectral information and 2D spatial information of a scene, resulting in significant savings in acquisition time and data storage. The reconstruction process decodes the 2D measurements to render a three-dimensional spatiospectral estimate of the scene, and is therefore an indispensable component of the spectral imager. Because often the scene to be reconstructed from the HSI data typically consists of spectrally and spatially homogeneous segments that can be represented sparsely in an appropriate basis, as is generally the case with SOI, we seek a particular form of the compressed sensing solution that assumes spectrally homogeneous segments in the two spatial dimensions, and greatly reduces the number of unknowns, often turning the under-determined reconstruction problem into one that is over-determined. Numerical tests are reported on both simulated and real data representing compressed measurements.

As an illustration we solve the joint reconstruction/segmentation problem by integrating a spectral signature solver with a segmentation solver - our fuzzy segmentation method for hyperspectral images. A sample result from this study, using a simulated hyperspectral image of the Hubble Space Telescope satellite developed in our papers (Gillis and Plemmons, 2011; Zhang, Wang, Plemmons, and Pauca, 2008), is given in Figure 17. Eight materials typical to those associated with satellites are used, Hubble aluminum, Hubble glue, Hubble honeycomb top, Hubble honeycomb side, solar cell, bolts, rubber edge, and copper stripping. Note the excellent recovery of six of the seven material spectra; the discrepancy between the estimated and true spectra for the bolts segment is related to its relatively small abundance in the object.

2.10 Coupled segmentation and denoising/deblurring methods

A crucial aspect of spectral image analysis is the identification of the materials present in the object or scene being imaged and to quantify their fractional abundances in the mixture. An increasingly useful approach to extracting such underlying structure is to employ image classification and object identification techniques to compressively represent the original data cubes by a set of spatially orthogonal bases and a set of spectral signatures. Owing to the increasing quantity of data usually encountered in hyperspectral data sets, effective data compressive representation is an important consideration, and noise and blur can present data analysis problems. We developed image segmentation methods for hyperspectral space object material identification and coupled the segmentation with a hyperspectral image data denoising/deblurring model to propose this method as an alternative to a tensor factorization methods proposed recently (Zhang, Wang, Plemmons, and Pauca, 2008). The model provides the segmentation result and the restored image simultaneously. Numerical results show the effectiveness of our proposed combined model in hyperspectral material identification (Li, Ng, and Plemmons, 2011).

2.11 Sparse Nonnegative Underapproximation for Hyperspectral Image Analysis

Dimensionality reduction techniques such as principal component analysis (PCA) are powerful tools for the analysis of high-dimensional data. In hyperspectral image analysis, nonnegativity of the data can be taken into account, leading to an additive linear model called nonnegative matrix factorization (NMF), which improves interpretability of the decomposition. Recently, another technique based on underapproximations (NMU) has been introduced, which allows the extraction of features in a recursive way, such as PCA, but preserving nonnegativity, such as NMF. Moreover, in some situations, NMU is able to detect automatically the materials present in the scene being imaged. However, for difficult hyperspectral datasets, NMU can mix some materials together, and is therefore not able to separate all of them properly. In this paper we introduce sparse NMU by adding a sparsity constraint on the abundance matrix and use it to extract materials individually in a more efficient way than NMU. This is experimentally demonstrated on the HYDICE images of the San Diego airport and the Urban dataset (Gillis and Plemmons, 2011).

3 Publications Citing Grant Funding Support

1. Prasad, S., "New Error Bounds for M-Testing and Estimation of Source Location with Sub-Pixel Precision," to appear in J. Opt. Soc. Am. A (2011).

2. Zhang, Q., Plemmons, R.J., Kittle, D., Brady, D., and Prasad, S., "Reconstructing and Segmenting Hyperspectral Images from Compressed Measurements," IEEE Conference on Remote Sensing, Lisbon, Portugal (2011). Available at `http://www.wfu.edu/ plemmons/papers/Wsegrec.pdf`

3. Kittle, D., Zhang, Q., Plemmons, R.J., Brady, D., and Prasad, S., "Joint Segmentation and Reconstruction of Coded Aperture Hyperspectral Data," *Computational Optical Sensing and Imaging (COSI)* Topical Meeting of the Optical Society of America, Toronto, Canada (July 2011). Abstract available at `http://www.opticsinfobase.org/abstract.cfm?URI=COSI-2011-CMD1`

4. Prasad, S., and Narravula, S., "Applications of Shannon information and statistical estimation theory to inverse problems in imaging," *Signal Recovery and Synthesis (SRS)* Topical Meeting of the Optical Society of America, Toronto, Canada (July 2011). Abstract available at `http://www.opticsinfobase.org/abstract.cfm?URI=SRS-2011-SMC1`

5. Zhang, Q., Plemmons, R.J., Kittle, D., Brady, D., and Prasad, S., "Joint Segmentation and Reconstruction of Hyperspectral Data from a Single Snapshot," Proc. SPIE Defense, Security and Sensing, Orlando, FL. Proc. of SPIE, vol. 8048 (2011). Limited availability at `http://spie.org/x648.html?productid=881777`

6. Prasad, S. and Zhang, Q., "Exploiting Spectral Correlations for Segmentation and Shape Determination from Hyperspectral Datacubes of Rotating Satellites," Advanced Maui Optical and Space Surveillance (AMOS) Technical Conference (Sep 2010). Available at `http://www.amostech.com/TechnicalPapers/2010.cfm`

7. Li, F., Ng, M., Plemmons, R.J., Prasad, S., and Zhang, Q., "Coupled Segmentation and Denoising/Deblurring Models for Hyperspectral Material Identification, Proc. SPIE Defense, Security and Sensing, vol. 7701, paper no. 7701-2 (2010).

8. Gillis, N., and Plemmons, R., "Dimensionality reduction, classification, and spectral mixture analysis using nonnegative underapproximation," Opt. Eng., Vol. 50, 027001 (Feb. 2011).

9. Gillis, N., and Plemmons, R., "Sparse Nonnegative Matrix Underapproximation and Its Application to Hyperspectral Image Analysis," Proc. IEEE WHISPERS Conference on Remote Sensing (2011). Available at `http://www.wfu.edu/~plemmons/papers.html`

10. Morigi, S., Plemmons, R., Reichel, L., and Sgallari, F., "A Hybrid Multilevel-active Set Method for large Box-constrained linear Discrete Ill-posed Problems," Calcolo, Vol. 48, pp. 89-105, 2011.

11. Li, F., Ng, M., and Plemmons, R., "Coupled Segmentation and Denoising/Deblurring Models for Hyperspectral Material Identification," Num. Lin. Alg. and Applic., to appear 2011.

12. Zhang, Q., Plemmons, R.J., Kittle, D., Brady, D. and Prasad, S. (2011) Joint segmentation and reconstruction of hyperspectral data from compressive measurements, Applied Optics, 50(22): 4286-4294 (2011).

13. Kittle, D., Marks, D., Brady, D. (2012) Design and fabrication of a snapshot-capable, UV-visible coded aperture spectral imager (CASI), Optical Engineering, special issue on computational imaging, in submission, 2012.

14. Kittle, D., Marks, D., Kim, M., Rushmeier, H., Brady, D. (2011) Design and Fabrication of a UV-Visible Coded Aperture Spectral Imager (CASI), OSA, Frontiers in Optics, San Jose, USA, 2011.

15. Deloye, C., Flake, J., Kittle, D., Bosch, E., Rand, R., and Brady, D. (2011) Exploitation Performance and Characterization of a Prototype Compressive Sensing Imaging Spectrometer, Pending publication in February Fourier Talks proceedings.

16. Kittle, D., Choi, K., Wagadarikar, A., Brady, D. (2010) Multiframe image estimation for coded aperture snapshot spectral imagers, Appl. Opt., 49: 6824-6833, 2010.

17. S. Prasad and D. Hope, "Information theoretic characterizations of compressive-sensing-based space object identification," Proc. of SPIE, vol. 7800, pp. 78000B-1:11 (2010).

18. Prasad, S., and Luo, X., "Support-assisted optical superresolution of low-resolution image sequences: The one-dimensional problem," Opt. Express, vol. 17, pp. 23213-23233 (2009).

19. Prasad, S., and Luo, X., "An information theoretic analysis of support assisted optical superresolution in one and two dimensions," Paper CTuC3 presented at the Computational Optical Sensing and Imaging Conference, San Jose, CA, Oct. 10-12, 2009. Available at `http://www.opticsinfobase.org/abstract.cfm?uri=COSI-2009-CTuC3`

20. Prasad, S., and Luo, X., "Support-based digital and optical superresolution in one and two dimensions," Proceedings of the 2009 AMOS Technical Conference, Maui, HI, Sep 1-4, 2009. Available at `http://www.amostech.com/TechnicalPapers/2009.cfm`

21. Hope, D., and Prasad, S., "A statistical information based analysis of a compressive imaging system," Proceedings of the 2009 AMOS Technical Conference,Maui, HI, Sep 1-4, 2009. Available at `http://www.amostech.com/TechnicalPapers/2009.cfm`

22. Zhang, Q., Guy, R., and Plemmons, R., "Matrix Structures and Parallel Algorithms for Image Superresolution Reconstruction," SIAM. J. Matrix Anal. and Applications, Vol.31(4), pp. 1873-1893 (2010).

23. Prasad, S., "PSF uncertainty and image estimation errors," Unconventional Imaging Conference, 2008 Annual SPIE Meeting, San Diego, CA, Aug 11, 2008: Proc. SPIE, vol. 6712, pp. 709407-1:12 (2008).

24. D. Chen and R. Plemmons, "Nonnegativity Constraints in Numerical Analysis," Paper presented at the Symposium on the Birth of Numerical Analysis, Leuven Belgium, October 2007. In The Birth of Numerical Analysis, World Scientific Press, A. Bultheel and R. Cools, Eds., pp. 109-140 (2009).

25. Zhang, Q., Wang, H., Plemmons, R., and Pauca, V.P., "Tensor Methods for Hyperspectral Data Analysis: A Space Object Material Identification Study," J. Opt. Soc. Am. A, Vol.25, No. 12, pp. 3001-3012 (2008).

4 Invited Presentations

1. S. Prasad presented "Applications of Shannon information and statistical estimation theory to inverse problems in imaging" at the Signal Recovery and Synthesis Topical Meeting of the Optical Society of America, Toronto, CA (July 11, 2011)

2. R. Plemmons presented "Combined Reconstruction and Segmentation of Hyperspectral Data" at Conference in Numerical Analysis: Theory, Methods and Applications, Chania, Crete, Greece, 2010.

3. R. Plemmons presented "Variational Models for Image Segmentation" at Mathematics in Image Processing, Guangzhou, China, 2010.

4. R. Plemmons presented "Variational PDE Methods for Imaging" at Conference on Inverse Problems, Computations, and Applications, Luminy, France, 2010.

5. R. Plemmons presented "Tensor Methods in Imaging" at International Conference on Structured Matrices and Applications, Hong Kong, China, 2010.

6. R. Plemmons presented "Spectral Trace Recovery for Material Identification using Variational Methods" at Interdisciplinary Workshop on Fixed-Point Algorithms for Inverse Problems in Science and Engineering, Banff, Alberta, Canada 2009.

7. R. Plemmons presented "Some Applications of Nonnegative Tensor Factorizations to Mining Hyperspectral Data" at NSF Workshop on Future Directions in Tensor-Based Computation and Modeling, Arlington, VA, 2009.

8. R. Plemmons presented "Tensor Decomposition Methods in Hyperspectral Data Analysis" at Conference on Applied Linear Algebra, SIAM, Monterey, CA, 2009.

9. R. Plemmons presented "Iterative Methods for Image Restoration" at NSF Conference on the Occasion of Richard Varga's 80th Birthday, Kent, Ohio, 2008.

5 Other Presentations

1. Q. Zhang presented "Joint Segmentation and Reconstruction of Hyperspectral Data from a Single Snapshot" at SPIE Conference on Defense, Security and Sensing, Orlando, FL, 2011.

2. D. Kittle presented "Joint Segmentation and Reconstruction of Coded Aperture Hyperspectral Data" at OSA, Computational Optical Sensing and Imaging, Toronto, Canada, 2011.

3. D. Kittle presented "Design and Fabrication of a UV-Visible Coded Aperture Spectral Imager (CASI)" at OSA, Frontiers in Optics, San Jose, USA, 2011.

4. R. Plemmons presented "Reconstructing and Segmenting Hyperspectral Images from Compressed Measurements" at IEEE Conference on Remote Sensing, Lisbon, Portugal, 2011.

5. R. Plemmons presented "Coupled Segmentation and Denoising/Deblurring Models for Hyperspectral Material Identification" at SPIE Conference on Defense, Security and Sensing, Orlando, FL, 2010.

6. R. Plemmons presented "Dimensionality Reduction, Classification, and Spectral Mixture Analysis using Nonnegative Underapproximation" at SPIE Conference on Defense, Security and Sensing, Orlando, FL, 2010. Named the best paper in the symposium on hyperspectral imaging.

7. S. Prasad presented "Exploiting Spectral Correlations for Segmentation and Shape Determination from Hyperspectral Datacubes of Rotating Satellites" at Advanced Maui Optical and Space Surveillance Technologies Conference, Maui, HI, 2010.

8. R. Plemmons presented "Nonnegativity Constraints in Scientific Computation" at 12th Householder Symposium, Berlin, Germany, 2008.

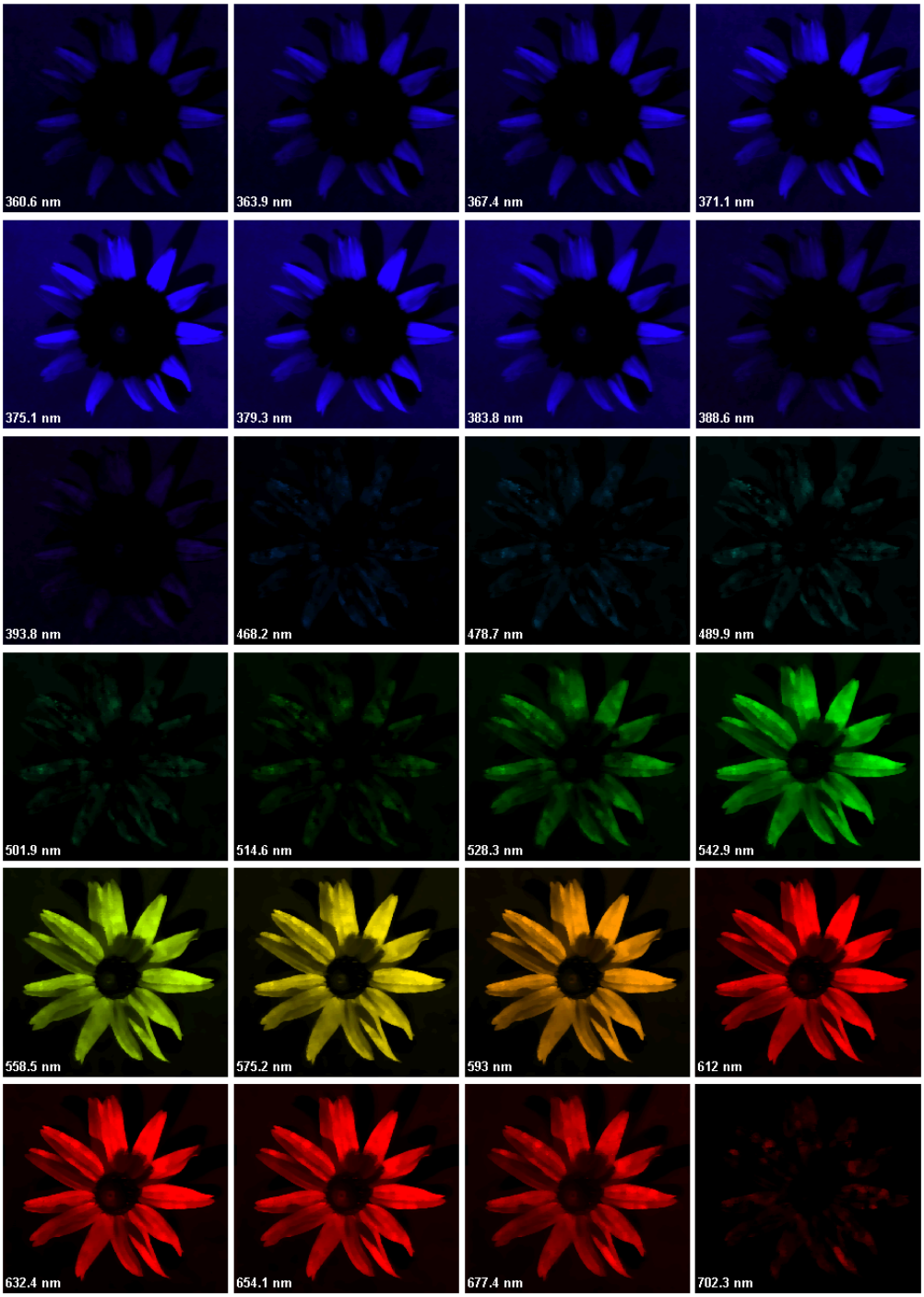

Figure 14: UV-Visible reconstruction from 360nm to 700nm, taken using multiple frames in direct sunlight.

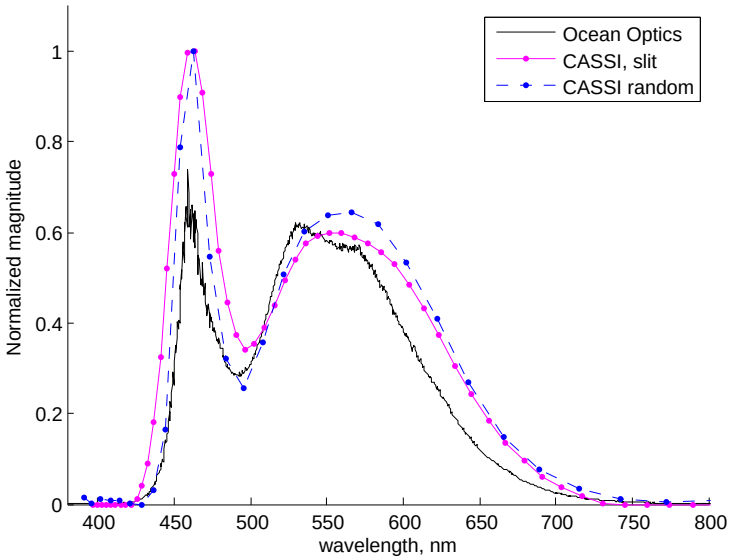

Figure 15: Comparison of the CASSI spectral resolution with a 1-pixel wide slit, 2-pixel feature random mask reconstructed with TwIST and 24-frames, and commercial Ocean Optics spectrometer. Both CASSI spectra are uncalibrated for quantum efficiency of the detector, optical transmission efficiency, and channel sensitivity.

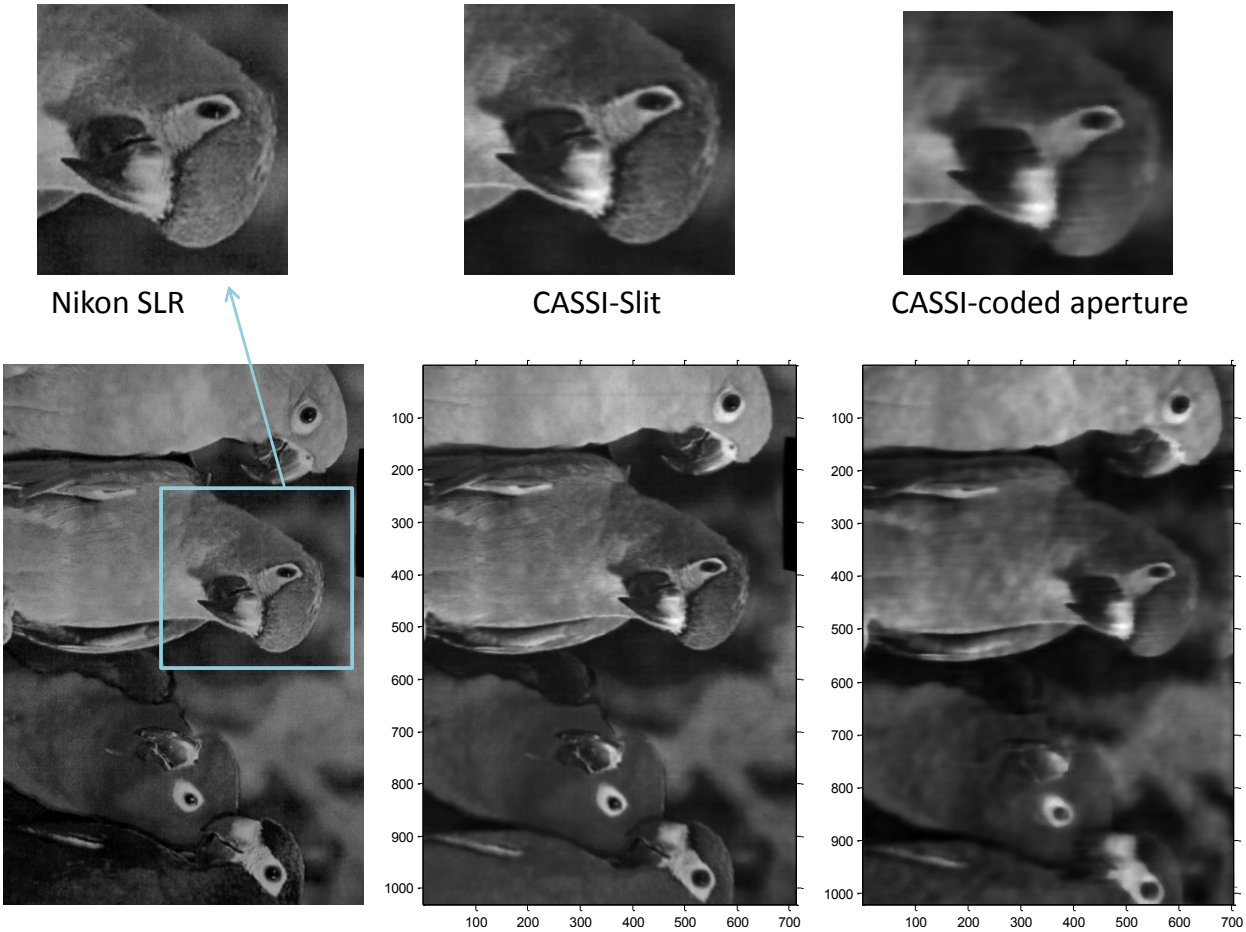

Figure 16: Comparison with a commercial Nikon SLR camera in monochrome, CASSI with the coded aperture replaced by a slit and pushbroomed, and a multiframe CASSI image. Acquisition time for the slit was around 20 minutes, for CASSI about 5 seconds.

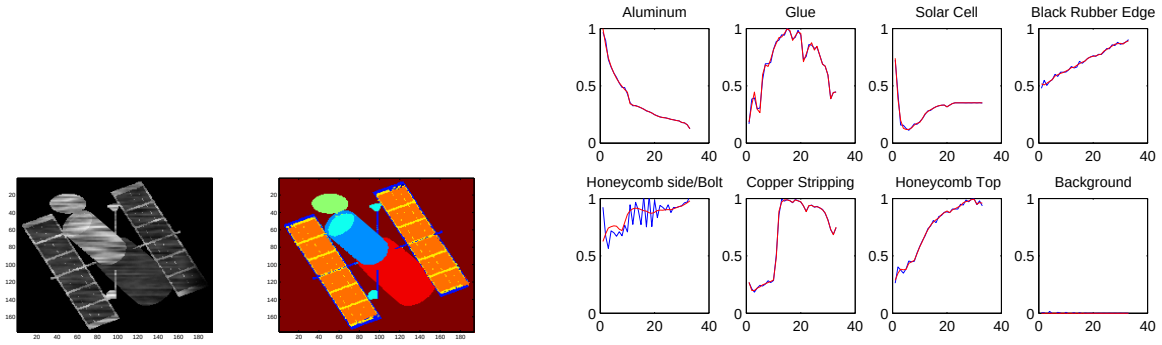

(a) (b) (c)

Figure 17: (a) Raw CASSI simulated compressed sensing image. (b) The reconstructed/segmented CASSI image. False color identifies the materials in the satellite. (c) The estimated material spectral signatures compared with the original ones.